AFRL-RX-WP-JA-2019-0059

CALPHAD-AIDED DEVELOPMENT OF QUATERNARY MULTI-PRINCIPAL ELEMENT REFRACTORY ALLOYS BASED ON NbTiZr (POSTPRINT)

O.N. Senkov, A.L. Pilchak, E.J. Payton, and C. Woodward

AFRL/RX

C. Zhang and F. Zhang

CompuTherm

30 NOVEMBER 2018
Interim Report

AIR FORCE RESEARCH LABORATORY
MATERIALS AND MANUFACTURING DIRECTORATE
WRIGHT-PATTERSON AIR FORCE BASE, OH 45433-7750
AIR FORCE MATERIEL COMMAND
UNITED STATES AIR FORCE

REPORT DOCUMENTATION PAGE

Form Approved
OMB No. 0704-0188

1. REPORT DATE *(DD-MM-YY)*	2. REPORT TYPE	3. DATES COVERED *(From - To)*
30 November 2018	Interim	19 March 2014 – 30 October 2018

4. TITLE AND SUBTITLE
CALPHAD-AIDED DEVELOPMENT OF QUATERNARY MULTI-PRINCIPAL ELEMENT REFRACTORY ALLOYS BASED ON NbTiZr (POSTPRINT)

5a. CONTRACT NUMBER
IN-HOUSE

5b. GRANT NUMBER

5c. PROGRAM ELEMENT NUMBER

6. AUTHOR(S)
1) O.N. Senkov, A.L. Pilchak, E.J. Payton, and C. Woodward- AFRL/RX
2) C. Zhang and F. Zhang – CompuTherm
(Continued on page 2)

5d. PROJECT NUMBER

5e. TASK NUMBER

5f. WORK UNIT NUMBER
X0W6

7. PERFORMING ORGANIZATION NAME(S) AND ADDRESS(ES)
1) AFRL/RX
Wright-Patterson AFB
Dayton, OH 45433
2) CompuTherm, LLC
8401 Greenway Blvd #248
Middleton, WI 53562
(Continued on page 2)

8. PERFORMING ORGANIZATION REPORT NUMBER

9. SPONSORING/MONITORING AGENCY NAME(S) AND ADDRESS(ES)
Air Force Research Laboratory
Materials and Manufacturing Directorate
Wright-Patterson Air Force Base, OH 45433-7750
Air Force Materiel Command
United States Air Force

10. SPONSORING/MONITORING AGENCY ACRONYM(S)
AFRL/RXCM

11. SPONSORING/MONITORING AGENCY REPORT NUMBER(S)
AFRL-RX-WP-JA-2019-0059

12. DISTRIBUTION/AVAILABILITY STATEMENT
DISTRIBUTION STATEMENT A. Approved for public release: distribution is unlimited.

13. SUPPLEMENTARY NOTES
PA Case Number: 88ABW-2018-6014; Clearance Date: 30 Nov 2018. This document contains color. Journal article published in Journal of Alloys and Compounds, Vol. 783, 28 Dec 2018. © 2018 Elsevier B.V. The U.S. Government is joint author of the work and has the right to use, modify, reproduce, release, perform, display, or disclose the work.
The final publication is available at https://doi.org/10.1016/j.jallcom.2018.12.325

14. ABSTRACT *(Maximum 200 words)*
Equilibrium phase diagrams for ten MeX(NbTiZr)100-X alloy systems, where Me is Al, Cr, Fe, Hf, Mo, Re, Si,Ta, V or W and X ranges from 0 to 25 at% were calculated using the PanNb2018a database recently developed by CompuTherm, LLC. By the type of phases and sequence of formation, these alloy systems can be divided into two groups. The first group of quaternary alloys, containing Al, Hf, Mo, Ta, or V has a single-phase BCC region below the solidus line over the entire X range and can be considered as potential candidates for the development of single-phase high entropy alloys. The second group consists of the quaternary alloy systems in which the fourth element (Cr, Fe, Re, Si or W) has limited solubility in BCC NbTiZr, which leads to the formation of an additional phase below the solidus and above the solubility limit. These quaternary alloy systems can be used for the development of precipitation or dispersoid strengthened complex concentrated alloys.

15. SUBJECT TERMS
Refractory alloys; phase diagrams; microstructure; mechanical properties

16. SECURITY CLASSIFICATION OF:			17. LIMITATION OF ABSTRACT:	18. NUMBER OF PAGES	19a. NAME OF RESPONSIBLE PERSON (Monitor)
a. REPORT	b. ABSTRACT	c. THIS PAGE			Matthew LeSaint
Unclassified	Unclassified	Unclassified	SAR	16	19b. TELEPHONE NUMBER *(Include Area Code)* (937) 255-3636

Journal of Alloys and Compounds 783 (2019) 729–742

Contents lists available at ScienceDirect

Journal of Alloys and Compounds

journal homepage: http://www.elsevier.com/locate/jalcom

CALPHAD-aided development of quaternary multi-principal element refractory alloys based on NbTiZr

O.N. Senkov [a, *], C. Zhang [b], A.L. Pilchak [a], E.J. Payton [a], C. Woodward [a], F. Zhang [b]

[a] Air Force Research Laboratory, Materials and Manufacturing Directorate, Wright-Patterson AFB, OH 45433, USA
[b] CompuTherm, LLC, Middleton, WI 53562, USA

ARTICLE INFO

Article history:
Received 8 November 2018
Received in revised form
17 December 2018
Accepted 27 December 2018
Available online 28 December 2018

Keywords:
Refractory alloys
Phase diagrams
Microstructure
Mechanical properties

ABSTRACT

Equilibrium phase diagrams for ten $Me_X(NbTiZr)_{100-X}$ alloy systems, where Me is Al, Cr, Fe, Hf, Mo, Re, Si, Ta, V or W and X ranges from 0 to 25 at% were calculated using the PanNb2018a database recently developed by CompuTherm, LLC. By the type of phases and sequence of formation, these alloy systems can be divided into two groups. The first group of quaternary alloys, containing Al, Hf, Mo, Ta, or V has a single-phase BCC region below the solidus line over the entire X range and can be considered as potential candidates for the development of single-phase high entropy alloys. The second group consists of the quaternary alloy systems in which the fourth element (Cr, Fe, Re, Si or W) has limited solubility in BCC NbTiZr, which leads to the formation of an additional phase below the solidus and above the solubility limit. These quaternary alloy systems can be used for the development of precipitation or dispersoid strengthened complex concentrated alloys. To verify CALPHAD calculations three representative alloys, $Cr_{10}Nb_{30}Ti_{30}Zr_{30}$, $Ta_{10}Nb_{30}Ti_{30}Zr_{30}$ and $Re_{10}Nb_{30}Ti_{30}Zr_{30}$, were prepared by arc melting. The alloy densities were 6.56, 7.81 and 7.85 g/cm^3, respectively. The phase compositions of the produced alloys agreed satisfactorily with CALPHAD calculations. Mechanical properties were also studied and compared with those of NbTiZr. At room temperature (RT) all the alloys showed high hardness exceeding 350 Hv and high compression yield stress exceeding 1000 MPa. RT compression ductility of Re and Ta containing alloys was above 50%, but Cr-containing alloy showed low ductility of 5%. With an increase in temperature ≥800 °C, compression strength decreased more rapidly for the Cr-containing alloy, which at 1200 °C became softer than NbTiZr. The least temperature dependence of the strength was observed for the Ta-containing alloy, which became the strongest at 1200 °C.

1. Introduction

Refractory complex concentrated alloys (RCCA), which also include refractory high entropy alloys (RHEAs), are one of the most recent developments in material science of structural materials. This class of alloys has attracted much attention due to vast, unexplored variations in alloy compositions with promising combinations of elevated temperature mechanical properties, reduced density and improved oxidation resistance relative to conventional refractory alloys [1–3]. At the present time, more than 100 RCCA systems and more than 150 RCCAs have been reported in the open literature. Some of the reported RCCAs have attractive combinations of relatively low density (down to 5.9 g/cm^3), high specific strengths and high melting temperature, which are superior to Ni-based superalloys [1–4]. These RCCAs generally consist of lower density refractory elements (Cr, Nb, V and/or Zr) and may also contain Al and/or Ti. Analysis of the composition of published RCCAs shows that more than half of them contain equiatomic concentrations of Nb, Ti and Zr [3].

The equiatomic ternary NbTiZr alloy is a single-phase BCC structure with a relatively low density of 6.63 g/cm^3. In the annealed condition, it has high hardness of 340 Hv, excellent room temperature ductility and impressive yield stress ($\sigma_{0.2} = 975$ MPa) [4]. Its strength, however, noticeably decreases with increasing temperature resulting in $\sigma_{0.2} = 123$ MPa at 1000 °C. This high temperature strength is still similar to a commercial refractory alloy C-103 [5], but at much lower density and cost. We therefore propose using NbTiZr as a baseline material for further refractory alloy developments and explore the effect of additions of other alloying elements on the microstructure and properties. To facilitate and

* Corresponding author.
E-mail address: oleg.senkov.ctr@us.af.mil (O.N. Senkov).

https://doi.org/10.1016/j.jallcom.2018.12.325
0925-8388/

accelerate the exploration, a CALPHAD approach is used to identify alloying elements which retain single-phase BCC solid solution and provide solid solution strengthening or produce additional solid solution or intermetallic phases, thus providing possibility for precipitation strengthening.

The present work uses a Nb thermodynamic database (PanNb2018a), which was developed and recently updated by CompuTherm, LLC, to analyze phase diagrams for $Me_X(NbTiZr)_{100-X}$ quaternary alloy systems (Me is the fourth element and X ranges from 0 to 25 at%) and identify attractive compositions for further studies. We have also produced three selected quaternary alloys, studied their phase composition, microstructure and mechanical properties and compared the experimental findings with the CALPHAD calculations.

2. Computational and experimental procedures

Equilibrium phase diagrams of $Me_X(NbTiZr)_{100-X}$ alloy systems, where Me is Al, Cr, Fe, Hf, Mo, Re, Si, Ta, V or W and X = 0 to 25 at.%, were calculated using the recently updated PanNb2018a thermodynamic database and Pandat software (version 2018) developed by CompuTherm, LLC [6]. The PanNb2018a database contains 13 elements listed above, 135 phases and has complete thermodynamic descriptions for all the binary systems, which build up the quaternary systems explored in this work. Among the 31 ternary alloy systems of interest to this work, only twelve of them, Al-Nb-Ti, Cr-Nb-Ti, Cr-Nb-Zr, Cr-Ti-Zr, Hf-Nb-Ti, Mo-Nb-Ti, Nb-Ta-Ti, Nb-Ti-Si, Nb-Re-Zr, Nb-Si-Zr, Nb-Ti-Zr and Ta-Ti-Zr, have complete thermodynamic assessment and two, Fe-Nb-Ti and Nb-Ti-W, have partial assessment. Therefore, when the ternary systems were unavailable, the calculations for the quaternary alloy systems were conducted by extrapolation from the binary systems [7,8]. It should be recognized that such extrapolation could lead to incorrect results if the ternary systems that are absent or not well assessed in the database contain ternary phases in nature [9]. The analyzed quaternary systems and the related ternary systems that have different levels of the thermodynamic description in the Nb database are given in Table 1. Complete thermodynamic description is available for the Cr-Nb-Ti-Zr system only. Si-Nb-Ti-Zr and Ta-Nb-Ti-Zr have three assessed ternaries, while Al-Nb-Ti-Zr, Hf-Nb-Ti-Zr, Mo-Nb-Ti-Zr, and Re-Nb-Ti-Zr have two fully assessed ternary systems. Fe-Nb-Ti-Zr and W-Nb-Ti-Zr have one fully assessed and one partially assessed ternary systems, while V-Nb-Ti-Zr has only one ternary system with complete thermodynamic description.

Based on the analysis of CALPHAD calculations, three quaternary alloys, $Ta_{10}Nb_{30}Ti_{30}Zr_{30}$, $Cr_{10}Nb_{30}Ti_{30}Zr_{30}$ and $Re_{10}Nb_{30}Ti_{30}Zr_{30}$, were selected and produced from high purity metals (purity of 99.9% or higher) by vacuum arc melting. To close solidification porosity, each alloy was wrapped in Ta foil and hot isostatic pressed (HIP'd) at 1400 °C by holding for 2 h under high-purity argon pressure of 276 MPa. After HIP, the alloys were additionally annealed at 1400 °C in 10^{-2} Pa vacuum for 6 h. The heating and cooling rates during HIP and annealing were ~20 °C/min or less. A ternary NbTiZr alloy was also produced and processed in identical conditions for comparison. The compositions of the alloys are shown in Table 2.

Table 1
Quaternary systems analyzed in this work and the related ternary systems that have complete, partial (p) or no thermodynamic description in Pan Nb2018a thermodynamic database.

Quaternary system	Complete or partial (p) ternary description	No ternary description
Al-Nb-Ti-Zr	Al-Nb-Ti; Nb-Ti-Zr	Al-Nb-Zr; Al-Ti-Zr
Cr-Nb-Ti-Zr	Cr-Nb-Ti; Cr-Nb-Zr; Cr-Ti-Zr; Nb-Ti-Zr	
Fe-Nb-Ti-Zr	Fe-Nb-Ti (p); Nb-Ti-Zr	Fe-Nb-Zr; Fe-Ti-Zr
Hf-Nb-Ti-Zr	Hf-Nb-Ti; Nb-Ti-Zr	Hf-Nb-Zr; Hf-Ti-Zr
Mo-Nb-Ti-Zr	Mo-Nb-Ti; Nb-Ti-Zr	Mo-Nb-Zr; Mo-Ti-Zr
Re-Nb-Ti-Zr	Nb-Re-Zr; Nb-Ti-Zr	Nb-Re-Ti; Ti-Re-Zr
Si-Nb-Ti-Zr	Nb-Si-Ti; Nb-Si-Zr; Nb-Ti-Zr	Si-Ti-Zr
Ta-Nb-Ti-Zr	Nb-Ta-Ti; Ta-Ti-Zr; Nb-Ti-Zr	Nb-Ta-Zr
V-Nb-Ti-Zr	Nb-Ti-Zr	Nb-Ti-V; Nb-V-Zr;Ti-V-Zr
W-Nb-Ti-Zr	Nb-Ti-W (p); Nb-Ti-Zr	Nb-W-Zr; Ti-W-Zr

Table 2
Density (in g/cm^3) and chemical composition (in at. %) of the produced alloys after heat treatment at 1400 °C.

Alloy	Density	Cr	Nb	Re	Ta	Ti	Zr
NbTiZr	6.63	0	36.3	0	0	32.2	31.5
$Ta_{10}Nb_{30}Ti_{30}Zr_{30}$	7.81	0	32.1	0	11.1	28.1	28.7
$Cr_{10}Nb_{30}Ti_{30}Zr_{30}$	6.56	8.7	34.4	0	0	29.2	27.7
$Re_{10}Nb_{30}Ti_{30}Zr_{30}$	7.85	0	32.6	10.3	0	27.7	29.4

The alloy density was measured using a helium pycnometer and the measured values are given in Table 2. Vickers microhardness was measured using a diamond pyramid applied to a polished surface of an alloy sample at 1000 g load for 15 s. X-ray diffraction was conducted using Cu $K_{\alpha 1}$ radiation in the 2θ range of 10–140°. Microstructural analysis was conducted using scanning electron microscopy (SEM) and electron backscatter diffraction (EBSD) techniques. Chemical composition was measured using energy dispersive spectrometer (EDS) attached to SEM.

Compression mechanical properties were determined in the temperature range from 25 °C to 1200 °C at a constant ram speed of 0.008 mm/s that corresponded to the initial strain rate of 10^{-3} s^{-1}. Compression specimens had a squared cross-section (5 mm × 5 mm) and the height of 8 mm. Room temperature tests were conducted in air and high-temperature tests were conducted in vacuum of ~2 10^{-3} Pa. A Teflon foil or boron-nitride powder coatings were used as lubricants between the sample and silicon-carbide dies during compression testing at room or elevated temperatures, respectively. The temperature program for high-temperature compression testing consisted of heating at 50 °C/min to a test temperature, holding at the temperature for 15 min, deformation with 55% height reduction (or until fracture, if it occurs first) and cooling at the initial cooling rate of 100 °C/min or the rate of furnace cooling, whichever is slower: no forced cooling was applied.

3. Results and discussion

3.1. CALPHAD phase analysis and alloy selection

3.1.1. Phase analysis

Equilibrium phase diagram projections for the NbTiZr-MeNbTiZr systems, where Me is Al, Cr, Fe, Hf, Mo, Re Si, Ta, V or W, are shown in Figs. 1 and 2. They can be divided into two groups.

The first group (Fig. 1) consists of the alloy systems containing Mo, Ta, V, Hf or Al. In these alloy systems a single-phase BCC region is present below the solidus line over the entire (0–25 at. %) composition range of the fourth element. Two solid solution phases, BCC+BCC or BCC+HCP, are present at lower temperatures in Mo, Ta and V containing systems (Fig. 1 a-c) or Hf-containing system (Fig. 1 d), respectively. One BCC phase is rich in Nb, as well as Mo, Ta or V, and the second BCC phase is rich in Ti and Zr, while the HCP phase is rich in Ti, Zr and Hf. Three different solid solution phases (two BCC and one HCP) and many intermetallic phases are present in the Al-containing quaternary system below the single-phase BCC field (Fig. 1 e). The presence of a wide single-phase

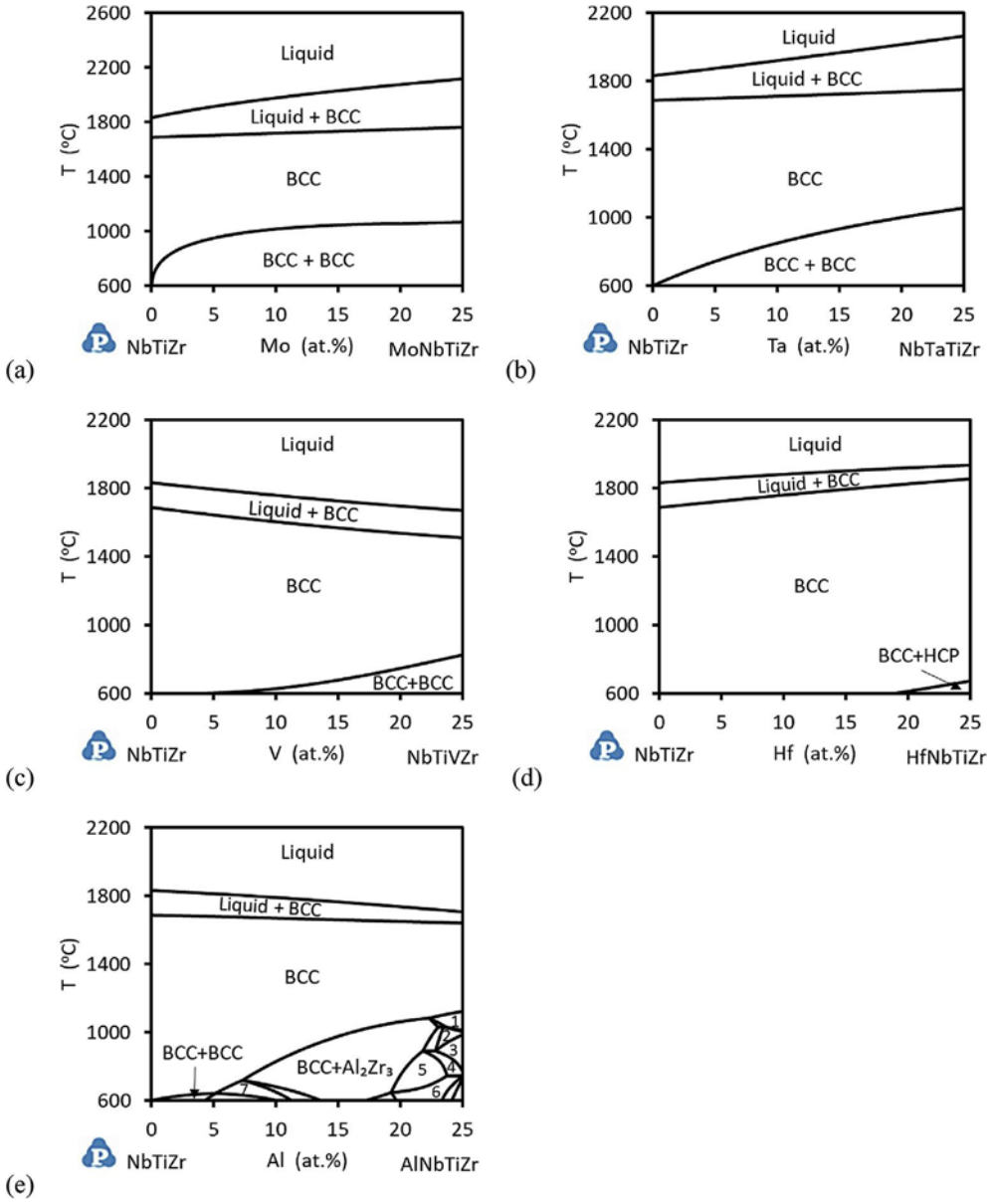

Fig. 1. Phase diagrams of (a) NbTiZr-MoNbTiZr, (b) NbTiZr-NbTaTiZr, (c) NbTiZr-NbTiVZr, (d) NbTiZr-HfNbTiZr and (e) NbTiZr-AlNbTiZr systems calculated using PanNb2018a database. The numbered phase fields in figure (e) are: 1- BCC+Al_4Zr_5, 2- BCC+Al_3Zr_4, 3- BCC+Nb_3Al+ Al_3Zr_4, 4- BCC+Nb_3Al+ Al_3Zr_4+Al_2Zr_3, 5- BCC+Nb_3Al+Al_2Zr_3, 6- Al_2Zr_3+BCC+HCP+Nb_3Al, 7- BCC+$AlZr_2$.

BCC region in these alloy systems makes them potential candidates for the development of single-phase high entropy alloys (HEAs) with higher number of components. Several 5-component single-phase BCC HEAs based on these elements, such as HfNbTaTiZr, HfMoNbTiZr and MoNbTaTiZr have already been reported [3], thus validating such approach.

The quaternary alloy systems of the second group (Fig. 2) have limited solubility of the fourth element (Cr, Fe, Re, Si or W) in BCC NbTiZr. Two phases, BCC+IM in Cr, Fe, Re or Si containing quaternary systems or BCC+BCC in W-containing system, are present below the solidus and above the solubility limit for the fourth element. Here IM is an intermetallic phase such as cubic Laves (C15) in Cr-containing system (Fig. 2a), hexagonal Laves (C14) in Fe or Re –containing systems (Fig. 2 a-c), and Zr_3Si in the Si-containing system (Fig. 2d). In the Cr, Fe, Re or Si containing quaternary systems, the BCC phase is rich in Nb and Ti, while the IM phase is rich in Cr, Fe, Re or Zr. A solid solution hexagonal phase containing more than 80%Zr is also identified in the $Fe_X(NbTiZr)_{100-X}$ at concentrations of Fe above ~17% and T < 800 °C (Fig. 2b). An additional BCC phase is present in $Re_X(NbTiZr)_{100-X}$ below 700 °C (Fig. 2c). In the W-containing system (Fig. 2e), one BCC phase is rich in Nb and W and another BCC phase is rich in Ti and Zr. A Laves (C15) phase is predicted at W concentrations ≥ 15 at. % and T < 1000 °C (Fig. 2e). The presence of the second phase up to very high temperatures, exceeding 1200 °C, as well as the presence of a high-temperature single-phase range in some of the alloys, makes these quaternary systems promising candidates for the development of precipitation- or dispersoid-strengthened HEAs capable to operate at temperatures beyond 1000 °C. Remarkable examples are a two-phase (B2+BCC) $AlMo_{0.5}Ta_{0.5}NbTiZr$, which has yield strength of 745 MPa at 1000 °C and 250 MPa at 1200 °C [10] and a three-phase (2BCC+Laves) $CrMo_{0.5}Ta_{0.5}NbTiZr$, which has yield strength of

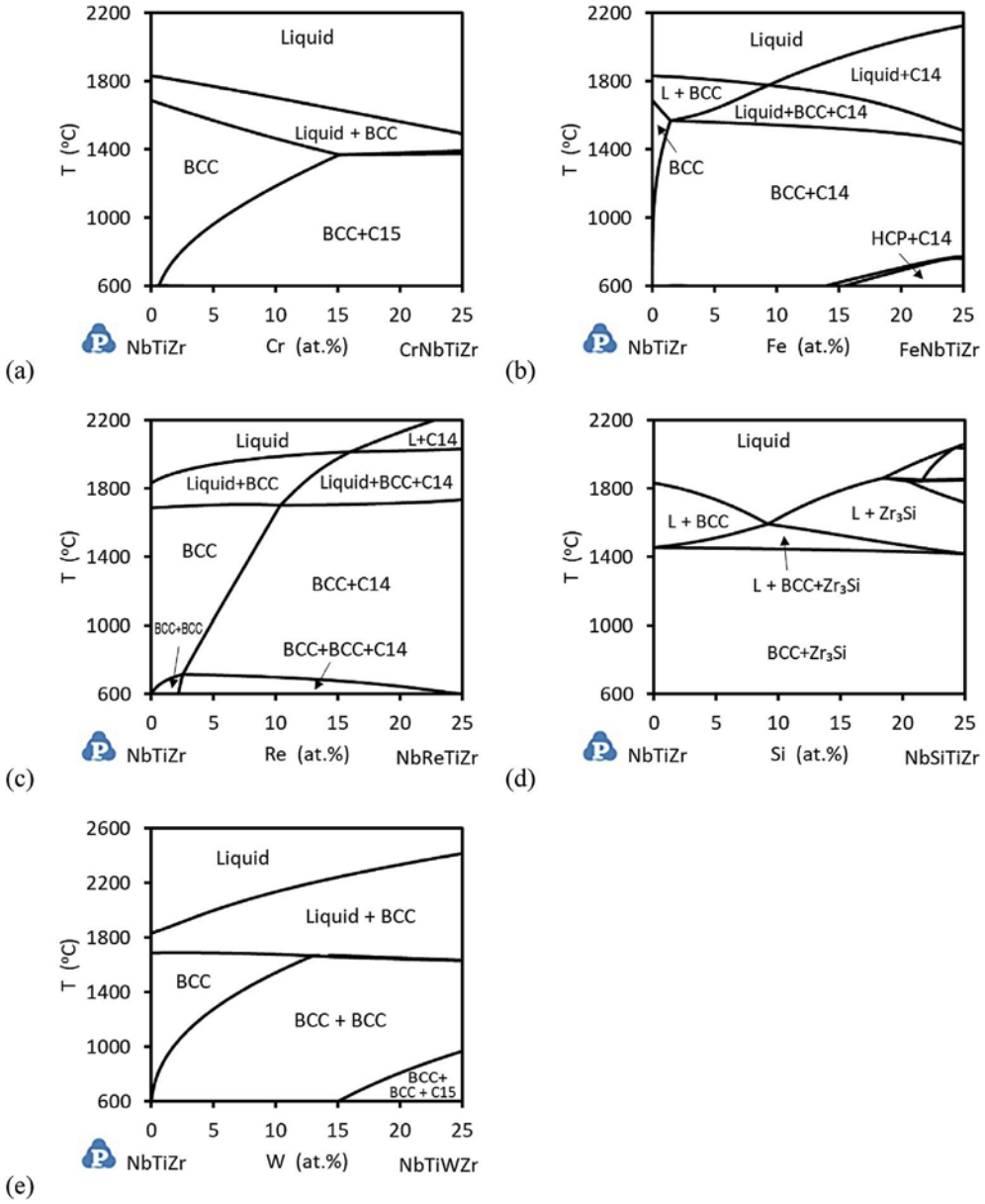

Fig. 2. Phase diagrams of (a) NbTiZr-CrNbTiZr, (b) NbTiZr-FeNbTiZr, (c) NbTiZr-NbReTiZr, (d) NbTiZr-NbSiTiZr and (e) NbTiZr-NbTiWZr systems calculated using PanNb2018a database.

546 MPa at 1000 °C and 170 MPa at 1200 °C [11].

Only 7 alloys from the analyzed quaternary systems have been experimentally evaluated and reported in open literature. These are NbTiZr [4,12,13], AlNbTiZr [14], CrNbTiZr [15–17], HfNbTiZr [18,19], MoNbTiZr [20,21], NbTaTiZr [22] and NbTiVZr [15–17]. X-ray and SEM/EDS analyses have shown that as-cast and annealed NbTiZr, HfNbTiZr and NbTaTiZr and as-cast MoNbTiZr are single-phase BCC structures; as-cast and annealed CrNbTiZr consists of BCC and cubic Laves (C15) phases, NbTiVZr contains two BCC phases and AlNbTiZr contains a BCC (ordered B2) and Al_3Zr_5 phases. These experimental results, except for MoNbTiZr and NbTaTiZr, are in fair agreement with the respective equilibrium phase diagrams given in Figs. 1 and 2. The calculations however predict the presence of two BCC phases in MoNbTiZr and NbTaTiZr below 1000 °C (Fig. 1 a, c). It should be noted that formation of low-temperature equilibrium phases can be kinetically restricted in these refractory alloys and long-time low-temperature annealing, often combined with plastic deformation, is required to validate these phases [23–27].

3.1.2. Alloy selection

Using the calculated phase diagrams, the following alloys were selected for more detailed analysis: $Ta_{10}Nb_{30}Ti_{30}Zr_{30}$, $Cr_{10}Nb_{30}Ti_{30}Zr_{30}$, $Si_{10}Nb_{30}Ti_{30}Zr_{30}$, $Si_4Nb_{32}Ti_{32}Zr_{32}$ and $Re_{10}Nb_{30}Ti_{30}Zr_{30}$. The calculated equilibrium phase diagrams for these alloys are given in Fig. 3 to Fig. 6.

The calculated phase fraction vs. temperature diagram of $Ta_{10}Nb_{30}Ti_{30}Zr_{30}$ is shown in Fig. 3a. A single-phase BCC region is present in a wide temperature range, from 850 °C to 1711 °C. The second BCC phase, in equilibrium condition, forms at relatively low temperature (the solvus temperature is 850 °C) and, therefore, if necessary, the phase separation can be restricted kinetically after annealing and/or thermo-mechanical processing in the single-phase BCC region [4,23]. On the other hand, if the alloy is expected for use at temperatures below ~700 °C, then its properties

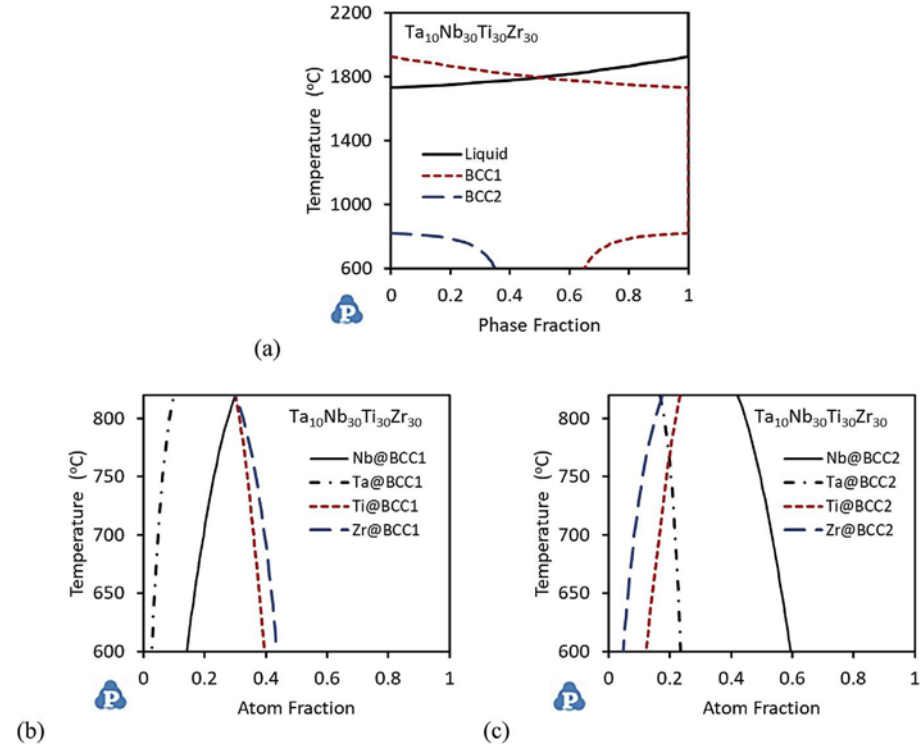

Fig. 3. (a) Calculated phase diagram and (b,c) temperature dependence of solubility of the alloying elements in (b) BCC1 and (c) BCC2 phases of $Ta_{10}Nb_{30}Ti_{30}Zr_{30}$.

can be modified through the solution treatment and precipitation of the second, BCC2 phase. With a decrease in temperature below the BCC2 solvus, the concentrations of Ti and Zr increase and that of Nb and Ta decrease in BCC1 (Fig. 3b), with a simultaneous decrease in the volume fraction of this phase to 63% at 600 °C (Fig. 3a). The BCC2 phase is rich in Nb, which concentration increases with decreasing temperature (Fig. 3c).

The second alloy, $Cr_{10}Nb_{30}Ti_{30}Zr_{30}$, has a single BCC phase at temperatures between 1185 °C (Laves phase solvus) and 1465 °C (solidus) and thus the ability for solution treatment by dissolution and re-precipitation of the Laves (C15) phase (Fig. 4a). A relatively low volume fraction (<16%) of the Laves phase can be beneficial for

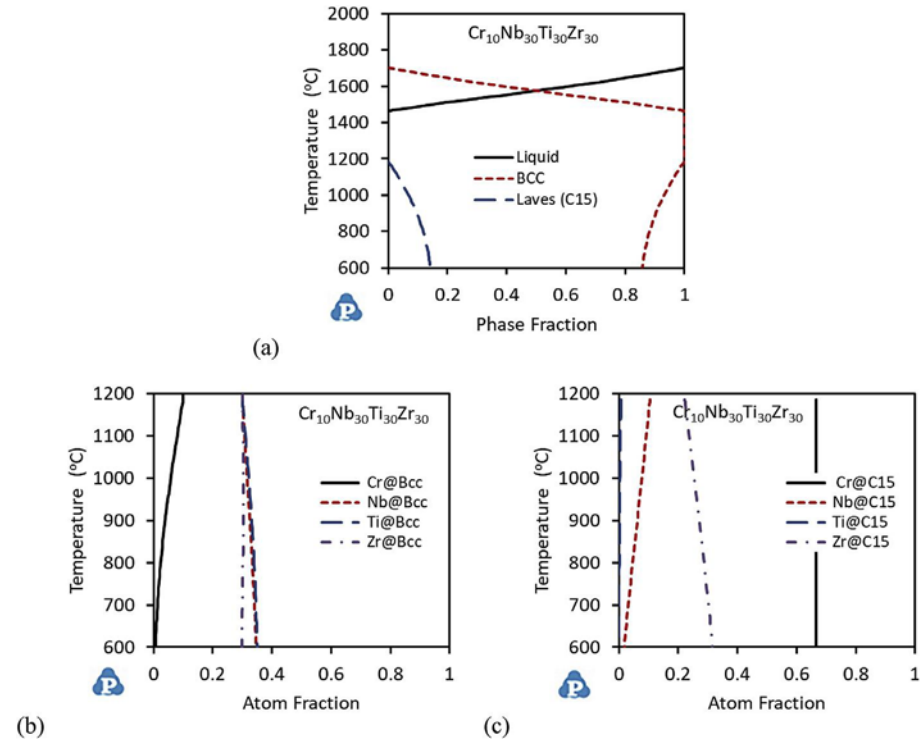

Fig. 4. (a) Calculated phase diagram and (b,c) temperature dependence of solubility of the alloying elements in (b) BCC and (c) Laves (C15) phases of $Cr_{10}Nb_{30}Ti_{30}Zr_{30}$.

the alloy ductility and workability while the strength can be controlled by C15 precipitation. The BCC phase in this alloy is rich in Nb and Ti (Fig. 4b) and C15 contains mainly Cr and Zr (Fig. 4c).

The calculated phase fraction vs. temperature diagrams of $Si_{10}Nb_{30}Ti_{30}Zr_{30}$ and $Si_4Nb_{32}Ti_{32}Zr_{32}$ are given in Fig. 5a and Fig. 5b, respectively. Because of no solubility of Si in BCC NbTiZr, the volume fraction of the second, silicide phase, $(Nb,Ti,Zr)_3Si$, does not change with an increase in temperature up to the eutectic reaction. This should provide thermal stability for the microstructure and mechanical properties. Moreover, presence of Si is expected to improve high-temperature corrosion resistance of these alloys [3,28]. In equilibrium conditions, the volume fraction of the silicide phase in $Si_{10}Nb_{30}Ti_{30}Zr_{30}$ and $Si_4Nb_{32}Ti_{32}Zr_{32}$ is predicted to be 0.4 and 0.16, respectively, and the eutectic reaction at 1446 °C and 1452 °C, respectively (Fig. 5 a, b). The concentration of Zr increases while that of Nb slightly decreases in the silicide phase with a decrease in temperature (Fig. 5c). The BCC phase has almost equiatomic concentration of Nb, Ti and Zr at temperatures above ~900 °C, while decreasing temperature below 900 °C increases the amount of Nb and decreases the amount Zr in the BCC phase. (Fig. 5d).

The calculated phase fraction vs. temperature diagram for $Re_{10}Nb_{30}Ti_{30}Zr_{30}$ is shown in Fig. 6a. The single-phase BCC range is narrow, between 1705 °C (solidus) and 1651 °C (Laves-phase solvus). Below 1651 °C, a hexagonal Laves (C14) phase forms which volume fraction increases almost linearly with decreasing temperature, approaching 0.2 at 600 °C. Below 700 °C, an additional BCC2 phase forms, which volume fraction approaches 0.2 at 600 °C, at the expense of the BCC1 phase. The BCC1 phase is rich in Nb, Ti and Zr at almost equal concentrations down to 700 °C and the Laves is rich in Re and Zr (Fig. 6 b, c). Formation of the Nb-rich BCC2 below 700 °C considerably reduces the amount of Nb and increases the amount of Zr in BCC1 (Fig. 6 b, d).

3.2. Experimental verification of CALPHAD calculations

To verify the correctness of the CALPHAD calculations based on the refined PanNb2018a database, 3 alloys, $Ta_{10}Nb_{30}Ti_{30}Zr_{30}$, $Cr_{10}Nb_{30}Ti_{30}Zr_{30}$, and $Re_{10}Nb_{30}Ti_{30}Zr_{30}$, were prepared and their phase compositions were studied after annealing at 1400 °C and after additional 55% compression deformation at 800 °C and 1000 °C. High temperature deformation has been found earlier facilitates decomposition of metastable phases toward equilibrium phases [3].

3.2.1. $Ta_{10}Nb_{30}Ti_{30}Zr_{30}$

According to X-ray diffraction, $Ta_{10}Nb_{30}Ti_{30}Zr_{30}$ is a single-phase BCC structure, both after annealing and after 55% compression at 800 °C and 1000 °C (Fig. 7a). The BCC lattice parameter is $a = 338.2 \pm 0.2$ pm. $Ta_{10}Nb_{30}Ti_{30}Zr_{30}$ has density of 7.81 ± 0.05 g/cm^3. SEM/BSE analysis identifies a homogeneous, coarse-grained structure (Fig. 7b), with the grain size over 1 mm. A very small fraction (less than 0.1%) of a Zr-rich second phase is found at grain boundaries (Fig. 7c). EDS analysis showed that this second phase consists of (in at.%) 27.1 Nb, 8.7 Ta, 22.4 Ti and 41.9 Zr Table 3, while the composition of the BCC matrix phase is similar to the alloy composition (Table 1).

After compression deformation at 1000 °C, $Ta_{10}Nb_{30}Ti_{30}Zr_{30}$ retains essentially single-phase BCC structure. Former grains become heavily deformed and a subgrain structure forms inside them (Fig. 7d). Fine recrystallized grains are present along the subgrain boundaries and along boundaries of former grains (Fig. 7 d, e). A negligible fraction of the Zr-rich precipitates retain at former grain boundaries, but they are fragmented into fine, round-shaped particles, probably due to localized dynamic recrystallization (Fig. 7e).

According to the calculated equilibrium phase diagram (Fig. 3a),

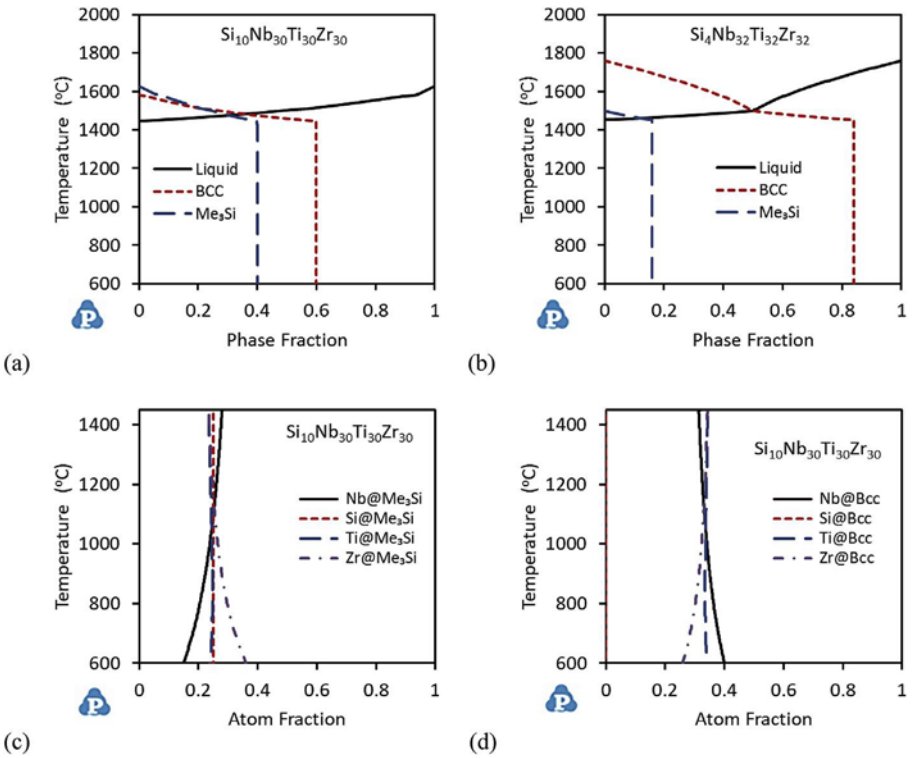

Fig. 5. (a,b) Calculated phase diagrams for $Si_{10}Nb_{30}Ti_{30}Zr_{30}$ and (b) $Si_4Nb_{32}Ti_{32}Zr_{32}$. (c,d) Temperature dependence of solubility of the alloying elements in (c) silicide phase and (b) BCC phase of $Si_{10}Nb_{30}Ti_{30}Zr_{30}$.

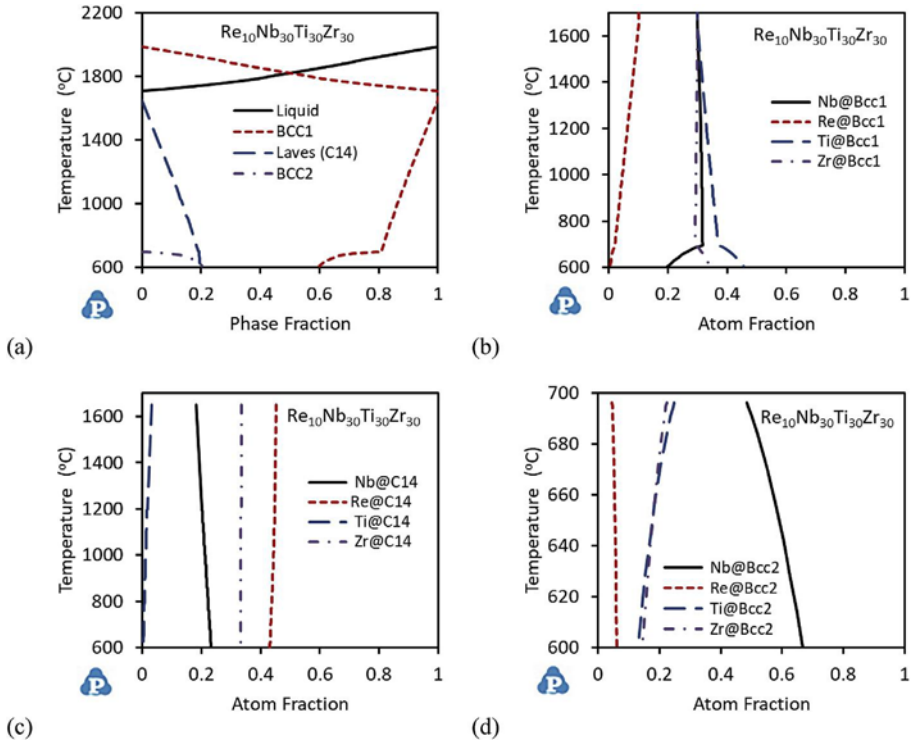

Fig. 6. (a) Calculated phase diagram and (b–d) temperature dependence of solubility of the alloying elements in (b) BCC1, (c) C14 and (d) BCC2 phases of $Re_{10}Nb_{30}Ti_{30}Zr_{30}$.

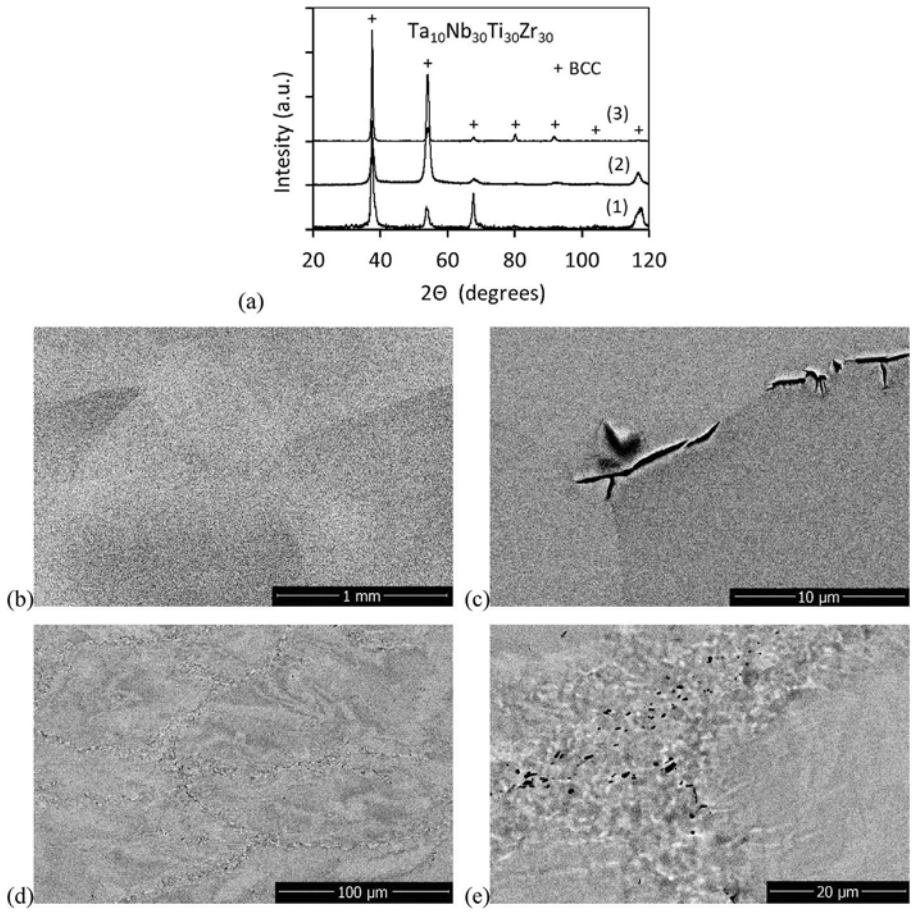

Fig. 7. $Ta_{10}Nb_{30}Ti_{30}Zr_{30}$ alloy: (a) X-ray diffraction patterns after annealing (1) and 55% compression deformation at 800 °C (2) and 1000 °C (3); (b–d) BSE images of the microstructure after (b,c) annealing and (d, e) 55% compression deformation at 1000 °C.

Table 3
Composition of a Zr-rich phase in $Ta_{10}Nb_{30}Ti_{30}Zr_{30}$, as it is determined experimentally or calculated using PanNb2018a database at 800 °C.

Composition	Nb	Ta	Ti	Zr
Experiment	27.1	8.7	22.4	41.9
CALPHAD, 800 °C	27.5	8.6	31.4	32.5

the experimentally observed single-phase BCC structure of $Ta_{10}Nb_{30}Ti_{30}Zr_{30}$ is likely metastable and corresponds to the high-temperature single-phase BCC range observed above 1000 °C. Because both annealing and deformation were conducted in the single-phase BCC range (at 1400 °C and 1000 °C, respectively), this indicates that the following cooling rate was not sufficiently low to accommodate diffusion-controlled phase decomposition, with the formation of a noticeable amount of the Zr-rich BCC2 phase at temperatures below 810 °C. The experimentally determined composition of the minor BCC2 agrees satisfactorily with the calculated equilibrium composition of the Zr-rich BCC1 phase at 800 °C, when the second phase has just started to form (Table 3). However, there is a critical discrepancy in the volume fraction of this phase: While the experiment indicates that the Zr-rich phase is the minor phase and its volume fraction is close to zero, CALPHAD calculations predict this phase to be a major phase with the volume fraction of ~0.91 (see Fig. 3 a, b). Our experimental results on $Ta_{10}Nb_{30}Ti_{30}Zr_{30}$ are in good agreement with recently reported results by Wang and Xu [29]. They found that an equimolar TaNbTiZr alloy is essentially a single-phase BCC structure that contains small amount of a Zr-rich BCC2 phase. The discrepancy between the experiments and CALPHAD calculations is likely due to incomplete assessment of ternaries in this quaternary alloy system (see Table 1). In particular, improvement may be obtained through inclusion of a thermodynamic description of Nb-Ta-Zr and modification of ternary interaction parameters for the Nb-Ta-Ti-Zr system to accommodate precipitation of a Zr-rich BCC2 phase, in agreement with the experimental data.

3.2.2. $Cr_{10}Nb_{30}Ti_{30}Zr_{30}$

X-ray diffraction indicates that the annealed $Cr_{10}Nb_{30}Ti_{30}Zr_{30}$ has a single-phase BCC structure, while the 800 °C and 1000 °C deformed alloy samples reveal the presence of two phases, BCC matrix and Laves (C15) precipitates (Fig. 8a). The lattice parameter of the BCC phase is $a = 334.1$ pm in the annealed condition and 337.1 pm in the 800 °C and 1000 °C deformed conditions. The lattice parameter of the Laves phase is $a = 717.9$ pm. Low-magnification BSE images of the annealed alloy show coarse grains of the matrix, with the average diameter of ~0.7 mm (Fig. 8b). Higher magnification BSE images expose needle-like precipitates inside grains and a chain of cuboidal particles at grain boundaries (Fig. 8c). The matrix phase is slightly depleted with Cr, while the composition of other elements is close to that of the alloy (Table 4). The second-phase precipitates are heavily rich in Cr and are identified (using EBSD) as a cubic (C15) Laves phase (Fig. 9). The alloy density is 6.56 ± 0.05 g/cm^3.

After deformation at 1000 °C, elongated, non-recrystallized

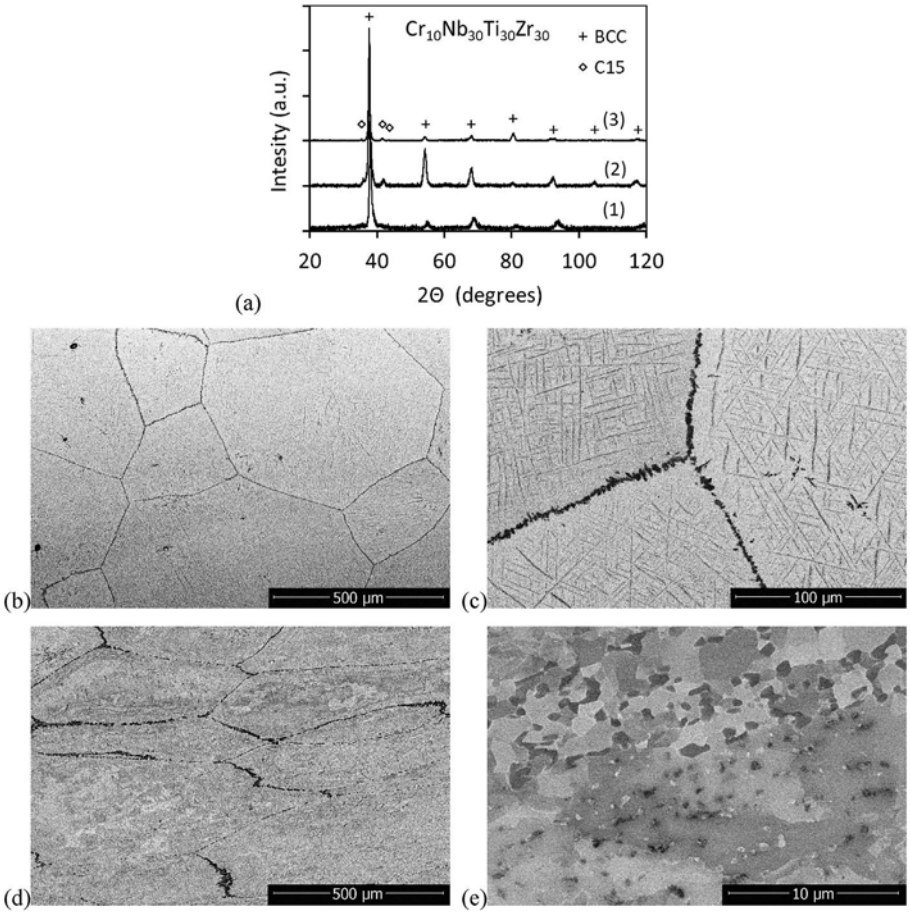

Fig. 8. $Cr_{10}Nb_{30}Ti_{30}Zr_{30}$ alloy: (a) X-ray diffraction patterns after annealing (1) and 55% compression deformation at 800 °C (2) and 1000 °C (3); (b–e) BSE images of the microstructure after (b,c) annealing and (d, e) 55% compression deformation at 1000 °C.

Table 4
Chemical composition (in at.%) of the constituents in $Cr_{10}Nb_{30}Ti_{30}Zr_{30}$ alloy after annealing at 1400 °C and after additional 55% compression deformation at 1000 °C.

Condition	1400 °C Annealed				1000 °C Deformed			
Constituent/Element	Cr	Nb	Ti	Zr	Cr	Nb	Ti	Zr
Alloy	9.0	34.4	28.7	27.9	8.4	34.5	29.6	27.5
BCC	7.1	34.8	29.7	28.4	4.3	36.5	32.7	26.5
Laves C15	45.7	16.3	12.5	25.5	44.2	17.4	13.2	25.2

Table 5
Chemical composition (in at.%) of the constituents in $Cr_{10}Nb_{30}Ti_{30}Zr_{30}$ alloy at 1060 °C and 1000 °C, as calculated by CALPHAD using Pandat Nb database.

Temperature	1060 °C				1000 °C			
Constituent/Element	Cr	Nb	Ti	Zr	Cr	Nb	Ti	Zr
Alloy	10	30	30	30	10	30	30	30
BCC	7.1	31.1	31.5	30.3	5.8	31.6	32.2	30.3
Laves C15	66.6	8.7	0.4	24.3	66.5	7.7	0.3	25.4

grains are clearly identified due to coarsening grain boundary precipitates. Fine subgrain structure forms inside the grains and original needle-like precipitates transform to near-globular particles (Figs. 8e and 9b). The composition of the matrix grain is only slightly different from the composition of the alloy, while the precipitates are rich in Cr (Table 4).

The experimental data are in satisfactory agreement with CALPHAD calculations. The experimentally determined composition and volume fraction of phases in the annealed condition roughly correspond to those predicted at ~1060 °C (the volume fraction of BCC is 0.95) and the composition and volume fraction of phases in 1000 °C deformed condition correspond to those predicted at 1000 °C (the volume fraction of BCC is 0.93) (Tables 4 and 5). The main disagreement between the experiment and calculations is in the composition of the Laves phase, for which CALPHAD calculations predict considerably higher amount of Cr (~66.5%) and considerably smaller amount of Nb and Ti than the experimentally observed. Similar difficulties in correct CALPHAD predictions of the composition of Laves or some other intermetallic phases were reported earlier [30–33]. It is worth noting that, in the PanNb2018a database, the Cr-Nb-Ti-Nb system has complete thermodynamic description for all four contained ternaries (Table 1) and thus good agreement of the CALPHAD calculations with the experimental data should be expected. The observed composition discrepancies for the Laves phase, however, indicate that the thermodynamic parameters related to this phase still need to be refined.

3.2.3. $Re_{10}Nb_{30}Ti_{30}Zr_{30}$

According to X-ray diffraction, $Re_{10}Nb_{30}Ti_{30}Zr_{30}$, both after annealing and high temperature deformation, consists of the matrix phase with a BCC crystal structure, which has lattice parameter $a = 334.8$ pm after annealing and $a = 335.3$ pm after 55% compression deformation at 800 °C or 1000 °C (Fig. 10a). A minor secondary phase is also present, which crystal structure, according to the positions of the diffraction peaks, can be equally identified as a hexagonal (C14) Laves, with the lattice parameters $a = 535.3$ pm and $c = 874.6$ pm, or a cubic (C15) Laves, with the lattice parameter $a = 757.3$ pm (Fig. 10a). BSE images support the presence of two phases, which have very different Z contrast (Fig. 10b). The BCC matrix phase has grey color and is slightly enriched with Ti and depleted in Re (Table 6). The average matrix grain size is ~75 μm. The second-phase particles are rich in Re and depleted in Ti and Nb and have bright color. They have cuboidal shape and are located at grain boundaries and also tend to form clusters inside grains (Fig. 10b). The volume fraction of these particles is estimated to be ~5.4%. EBSD imaging was not able to identify the Laves type of the second phase providing similar image quality for both C14 and C15 structures. Following the CALPHAD calculations it is assumed that the second phase has a hexagonal crystal structure. The $Re_{10}Nb_{30}Ti_{30}Zr_{30}$ alloy density is 7.85 ± 0.05 g/cm^3.

After compression deformation at 1000 °C, a cellular structure forms (Fig. 10c). The cells are elongated in the directions of plastic flow and the secondary particles are located in the channels between the cells (Figs. 10c and 11). EBSD analysis shows that the cells consist of non-recrystallized elongated matrix grains and the channels between the cells consist of fine, dynamically recrystallized grains (Fig. 11 a,b). It is likely that during deformation at 1000 °C dynamic recrystallization with formation of a fine-grain structure was facilitated in the matrix regions enriched with second-phase particles. Deformation was then localized in these fine-grain regions forming continuous recrystallized regions surrounding large, non-recrystallized grains. The volume fraction of the second-phase particles is estimated to be ~10.0%. The volume fraction of the dynamically recrystallized matrix (darker regions in Fig. 10c) is 31.4% and the volume fraction of non-recrystallized regions is 58.6%. After 1000 °C deformation, the concentration of Re in the second-phase particles slightly decreases (Table 6).

The experimentally determined phases and phase compositions

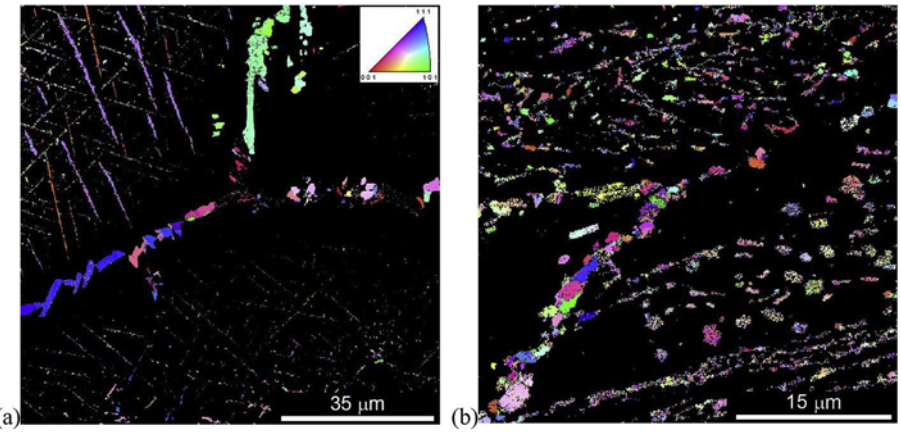

Fig. 9. EBSD inverse pole figure maps of grains of the Laves C15 phase in $Cr_{10}Nb_{30}Ti_{30}Zr_{30}$ alloy samples in (a) annealed condition and (b) deformed at 1000 °C condition. The color-coded crystal orientation triangle is shown as an insert in figure (a). The BCC (matrix) phase is black. (For interpretation of the references to color in this figure legend, the reader is referred to the Web version of this article.)

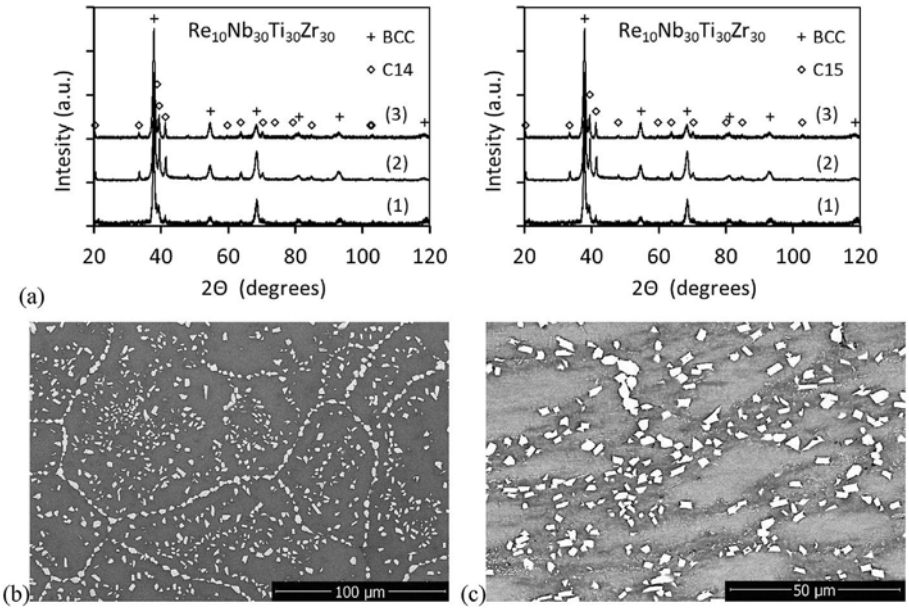

Fig. 10. $Re_{10}Nb_{30}Ti_{30}Zr_{30}$ alloy: (a) X-ray diffraction patterns after annealing (1) and 55% compression deformation at 800 °C (2) and 1000 °C (3); (b–c) BSE images of the microstructure after (b) annealing and (c) 55% compression deformation at 1000 °C.

Table 6
Chemical composition (in at.%) of the constituents in $Re_{10}Nb_{30}Ti_{30}Zr_{30}$ alloy after annealing at 1400 °C and additional 55% compression deformation at 1000 °C.

Condition	1400 °C Annealed				1000 °C Deformed			
Constituent/Element	Re	Nb	Ti	Zr	Re	Nb	Ti	Zr
Alloy	10.7	32.4	28.1	28.8	10.0	33.2	27.9	28.9
Matrix	8.6	33.2	30.1	28.1	9.4	33.0	29.4	28.2
Particles	36.0	15.2	18.0	30.8	34.5	15.9	18.1	31.5

in $Re_{10}Nb_{30}Ti_{30}Zr_{30}$ agree well with CALPHAD calculations, although only two of four ternaries related to the Re-Nb-Ti-Zr system have complete thermodynamic description in the PanNb2018a database used in this work. For example, the experiment reveals the presence of two phases, one of which (matrix) has a BCC crystal structure and another has been identified as a Laves phase, which volume fraction is 5.4% or 10% in the 1400 °C annealed or 1000 °C deformed conditions, respectively. At the same time, CALPHAD calculations predict the presence of two phases, BCC and hexagonal Laves (C14), with the volume fraction of C14 of 5.4% at 1400 °C and 13.6% at 1000 °C. Table 6 shows element compositions of the BCC matrix and second-phase particles in the 1400 °C annealed and 1000 °C deformed samples, and these experimental values are comparable with the compositions of the BCC1 and C14 phases calculated at respective temperatures (Table 7). The main disagreement is in the amount of Ti in the second-phase particles. While the experiment shows ~18% Ti in both annealed and deformed conditions, CALPHAD predicts only 2.2%Ti at 1400 °C and 1.1% Ti at 1000 °C in the Laves phase. The absence of secondary, BCC2 phase, which is predicted by CALPHAD at $T \leq 700$ °C, may

Table 7
Chemical composition (in at.%) of the constituents in $Re_{10}Nb_{30}Ti_{30}Zr_{30}$ alloy at 1400 °C and 1000 °C, as calculated by CALPHAD using PanNb2018a database.

Condition	1400 °C				1000 °C			
Constituent/Element	Re	Nb	Ti	Zr	Re	Nb	Ti	Zr
Alloy	10	30	30	30	10	30	30	30
BCC1	8.0	30.6	31.6	29.8	4.6	31.4	34.5	29.5
Laves C14	45.1	19.3	2.2	33.4	44.3	21.2	1.1	33.4

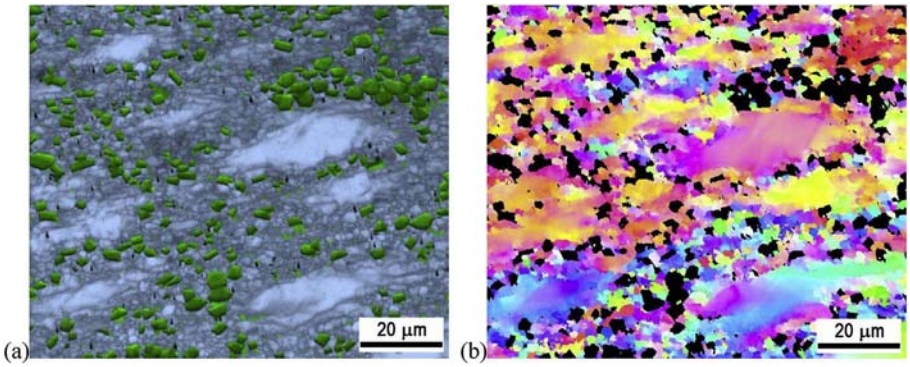

Fig. 11. EBSD images of $Re_{10}Nb_{10}Ti_{10}Zr_{10}$ alloy after 55% compression deformation at 1000 °C: (a) Combination of image quality and phase maps (BCC matrix is light-blue and Laves precipitates are green); (b) inverse pole figure map of the BCC matrix (the secondary precipitates are black). (For interpretation of the references to color in this figure legend, the reader is referred to the Web version of this article.)

indicate that it is kinetically restricted due to relatively low temperatures required for its formation.

3.3. Microhardness and compression properties

The baseline NbTiZr has Vickers microhardness of 340 Hv (Table 8). Addition of 10 at.% Ta slightly increases microhardness to 357 Hv, due to solution hardening. Microhardness of the two-phase $Cr_{10}Nb_{30}Ti_{30}Zr_{30}$ and $Re_{10}Nb_{30}Ti_{30}Zr_{30}$ alloys is noticeably higher, 457 Hv and 414 HV, respectively, likely resulting from the combined effects of solid solution and precipitation strengthening.

Compression deformation was conducted at 25 °C, 800 °C, 1000 °C, and 1200 °C and the true stress vs. true strain curves are shown in Fig. 12. The true yield stress ($\sigma_{0.2}$), peak stress (σ_p), peak strain (ε_p) and fracture strain (ε_f) values are given in Table 9.

At room temperature the baseline NbTiZr has $\sigma_{0.2} = 975$ MPa. This alloy shows yield stress drop at the beginning of deformation followed by continuous strain hardening and no evidence of fracture after true strain $\varepsilon = 70\%$. $Cr_{10}Nb_{30}Ti_{30}Zr_{30}$ has considerably higher $\sigma_{0.2}$ of 1586 MPa. After yielding, true stress of $Cr_{10}Nb_{30}Ti_{30}Zr_{30}$ increases rapidly to $\sigma_p = 1601$ MPa at $\varepsilon_p = 2.3\%$ and then rapidly decreases until fracture occurring at $\varepsilon_f = 5\%$. $Ta_{10}Nb_{30}Ti_{30}Zr_{30}$ and $Re_{10}Nb_{30}Ti_{30}Zr_{30}$ alloys have good room temperature ductility showing true fracture strains of 64% and 53%, respectively. While the Re addition increases $\sigma_{0.2}$ to 1196 MPa, Ta addition decreases $\sigma_{0.2}$ to 882 MPa, relative to the NbTiZr property. Both the alloys show strain hardening until $\varepsilon_p = 30–31\%$ followed by strain softening, with the peak stress values of 1211 MPa and 1628 MPa for $Ta_{10}Nb_{30}Ti_{30}Zr_{30}$ and $Re_{10}Nb_{30}Ti_{30}Zr_{30}$, respectively.

Table 9
Compression properties of the studied alloys: true yield stress ($\sigma_{0.2}$), true peak stress (σ_p), true peak strain (ε_p) and true fracture strain (ε_f). Apparent activation energies (Q/n and Q) determined at temperatures 800–1200 °C are also shown.

Alloy	NbTiZr	$Ta_{10}Nb_{30}Ti_{30}Zr_{30}$	$Cr_{10}Nb_{30}Ti_{30}Zr_{30}$	$Re_{10}Nb_{30}Ti_{30}Zr_{30}$
T = 25 °C				
$\sigma_{0.2}$ (MPa)	975	882	1576	1244
σ_p (MPa)	>1460	1211	1601	1628
ε_p (%)	>70	31	2.3	30
ε_f (%)	>70	64	5.0	53
T = 800 °C				
$\sigma_{0.2}$ (MPa)	465	596	580	805
σ_p (MPa)	474	652	632	906
ε_p (%)	0.95	2.4	1.7	3.0
ε_f (%)	>72	>72	>72	>72
T = 1000 °C				
$\sigma_{0.2}$ (MPa)	146	274	139	323
σ_p (MPa)	148	278	150	337
ε_p (%)	0.62	1.0	1.7	1.7
ε_f (%)	>76	>76	>76	>76
T = 1200 °C				
$\sigma_{0.2}$ (MPa)	61	102	37	89
σ_p (MPa)	63	103	40	89
ε_p (%)	0.62	0.89	2.3	0.87
ε_f (%)	>78	>78	>78	>78
T = 800°C-1200 °C				
Q/n (kJ/mol)	66.7	57.2	89.9	71.7
Q (kJ/mol)	333	286	449	356

At T = 800 °C–1200 °C all the studied alloys are ductile and do not show any macroscopic evidence of fracture up to true strains of 72–78%, when deformation stopped. In this temperature range the

Table 8
Vickers microhardness of the studied alloys after HIP and annealing at 1400 °C.

Alloy	NbTiZr	$Ta_{10}Nb_{30}Ti_{30}Zr_{30}$	$Cr_{10}Nb_{30}Ti_{30}Zr_{30}$	$Re_{10}Nb_{30}Ti_{30}Zr_{30}$
Microhardness (Hv)	340 ± 3	357 ± 3	457 ± 13	414 ± 8

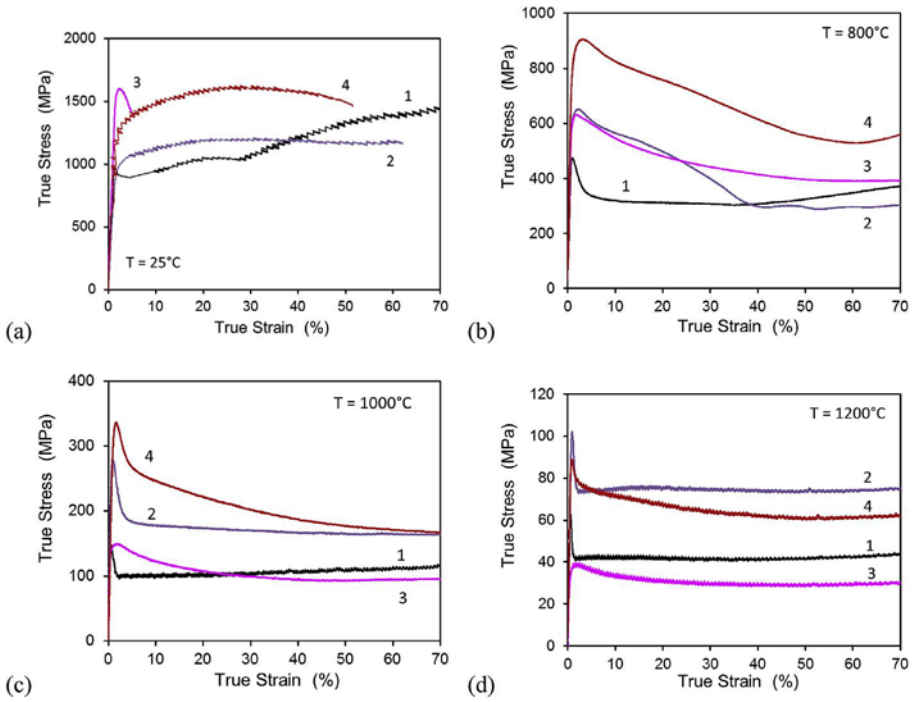

Fig. 12. True strain vs, true stress curves of (1) NbTiZr, (2) $Ta_{10}Nb_{30}Ti_{30}Zr_{30}$, (3) $Cr_{10}Nb_{30}Ti_{30}Zr_{30}$ and (4) $Re_{10}Nb_{30}Ti_{30}Zr_{30}$ alloys during compression deformation at (a) 25°C, (b) 800 °C, (c) 1000 °C and (d) 1200 °C.

alloys show peak stress at the beginning of deformation followed by strain-induced softening, which continues until the end of deformation or precedes steady state flow (Fig. 12b-d). Yield stress of the alloys at 800 °C is considerably smaller than at 25 °C (Table 9). The most pronounced drop in $\sigma_{0.2}$, by 2.7 times, occurs for $Cr_{10}Nb_{30}Ti_{30}Zr_{30}$, for which $\sigma_{0.2}$ at 800 °C is 580 MPa. The smallest drop in $\sigma_{0.2}$, by 1.5 times, is observed for $Ta_{10}Nb_{30}Ti_{30}Zr_{30}$ and $Re_{10}Nb_{30}Ti_{30}Zr_{30}$; for these two alloys $\sigma_{0.2}$ at 800 °C is 596 MPa and 805 MPa, respectively. NbTiZr has the smallest $\sigma_{0.2} = 465$ MPaat 800 °C.

At 1000 °C, $Re_{10}Nb_{30}Ti_{30}Zr_{30}$ and $Ta_{10}Nb_{30}Ti_{30}Zr_{30}$ are the strongest and second strongest alloys, with $\sigma_{0.2} = 323$ MPa and 274 MPa, respectively, while the smallest $\sigma_{0.2} = 139$ MPa is observed for $Cr_{10}Nb_{30}Ti_{30}Zr_{30}$. At 1200 °C, only $Ta_{10}Nb_{30}Ti_{30}Zr_{30}$ has $\sigma_{0.2}$ exceeding 100 MPa. The most pronounced decrease in the yield stress in this temperature range occurs in $Cr_{10}Nb_{30}Ti_{30}Zr_{30}$, which has mediocre $\sigma_{0.2} = 37$ MPa at 1200 °C (Fig. 12d, Table 9).

These results indicate that the two-phase $Cr_{10}Nb_{30}Ti_{30}Zr_{30}$ and $Re_{10}Nb_{30}Ti_{30}Zr_{30}$ are stronger than the single-phase NbTiZr and $Ta_{10}Nb_{30}Ti_{30}Zr_{30}$ at room temperature. However, with increasing temperature the two-phase alloys lose strength more rapidly than the single-phase alloys. Recent analysis of the deformation behavior of 37 RCCAs for which compression properties at 1000 °C had been reported showed similar tendency [3]. Namely it was found that multi-phase RCCAs generally have higher room temperature strength than single-phase BCC RCCAs; however, the advantage is lost at 1000 °C. Moreover, a multi-phase RCCA with the same RT $\sigma_{0.2}$ as a single-phase RCCA generally has a considerably smaller $\sigma_{0.2}$ at 1000 °C than the respective single-phase RCCA [3]. This trend suggests that achieving high strength at high temperatures in RCCAs does not necessarily require multi-phase structures and solid solution strengthening probably plays a primary role in these alloys at high temperatures.

The rapid decrease in the flow stress in Re and, especially, Cr containing quaternary alloys with an increase in temperature can be explained by a decrease in the volume fraction of the secondary (Laves) phase. For example, the volume fraction of the Laves phase in $Cr_{10}Nb_{30}Ti_{30}Zr_{30}$ decreases from 11.7% at 800 °C to 6.8% at 1000 °C, and 0% at ≥1185 °C (Fig. 4). In $Re_{10}Nb_{30}Ti_{30}Zr_{30}$, the Laves volume fraction decreases from 17% at 800 °C to 8.6% at 1000 °C and 3.6% at 1200 °C (Fig. 6). Additionally, the melting temperature of Cr is considerably lower than that of Re or Ta. Therefore, at T ≥ 1000 °C Cr is expected to be more mobile than Re and Ta in the NbTiZr matrix thus facilitating dislocation activity at lower stress levels.

The temperature dependence of the yield stress for the studied alloys is shown in Fig. 13 in the form of an Arrhenius plot, $\ln(\sigma_{0.2})$ vs. T^{-1}, where T is the absolute temperature. Two distinct temperature regions are clearly recognized (Fig. 13a). At temperatures between 298 and 1073 K (25–800 °C), the temperature dependence of $\sigma_{0.2}$ is much weaker than above 1073 K (800 °C).

Above 1073 K, a linear dependence of $\ln(\sigma_{0.2})$ on T^{-1} is observed (Fig. 13b). Similar behavior was earlier reported for a HfNbTaTiZr HEA [34]. Assuming conventional dependence of $\sigma_{0.2}$ on strain rate and temperature in the high-temperature range [35,36],

$$\sigma_{0.2}^{n} = A\dot{\varepsilon}\exp(Q/RT) \quad (1)$$

where $\dot{\varepsilon}$, n, Q, R and A are the strain rate, stress exponent, apparent activation energy, Gas constant, and materials dependent parameter, respectively. Q/n values for each of the studied alloys were determined from the temperature dependence of $\ln(\sigma_{0.2})$ (Fig. 13b) and they are given in Table 9. The results show that at T ≥ 800 °C, $Ta_{10}Nb_{30}Ti_{30}Zr_{30}$ has the weakest and $Cr_{10}Nb_{30}Ti_{30}Zr_{30}$ has the strongest temperature dependence of $\sigma_{0.2}$, with Q/n = 57.2 kJ/mol and 89.9 kJ/mol, respectively. For many metals and alloys deformed at high temperatures, n ≈ 5 [37]. Similar n-value was also reported for HfNbTaTiZr [34]. Using n = 5 for the current alloys, the apparent activation energies Q were estimated and are given in Table 9. It is found that Q ≈ 333 kJ/mol for NbTiZr and it increases with addition of Re (356 kJ/mol) or Cr (449 kJ/mol) and decreases with addition of Ta (286 kJ/mol). Higher Q values determined for the two-phase $Cr_{10}Nb_{30}Ti_{30}Zr_{30}$ and $Re_{10}Nb_{30}Ti_{30}Zr_{30}$, than for single-phase NbTiZr and $Ta_{10}Nb_{30}Ti_{30}Zr_{30}$, are probably due to a temperature-dependent decrease in the volume fraction of the secondary phase in this temperature range [38]. Additional mechanical testing at different strain rates is required to properly identify *n* values for each of the alloys. Additional microstructural studies on TEM level are also needed to identify deformation and strengthening mechanisms in these alloys. These are planned for future work.

4. Summary and conclusions

1 Phase diagrams of 10 quaternary alloy systems, $Me_X(NbTiZr)_{100-X}$, where Me is Al, Cr, Fe, Hf, Mo, Re, Si, Ta, V or W and X = 0 to 25 at.% were analyzed using the PanNb2018a thermodynamic database recently developed by CompuTherm LLC. The quaternary alloy systems containing Al, Hf, Mo, Ta, or V have a single-phase BCC region below the solidus line over the entire X range due to high solubility of these elements in NbTiZr. At temperatures below 700–1000 °C, the high-temperature BCC phase decomposes in two BCC phases in Mo, Ta or V containing alloys, BCC and HCP phase in Hf-containing alloys, or two BCC and several intermetallic (IM) phases in Al-containing alloys. The phase decomposition temperature increases with an increase in the concentration of the fourth element, as well as with the type of the element in the following order: Hf, V, Ta, Mo, Al. The other

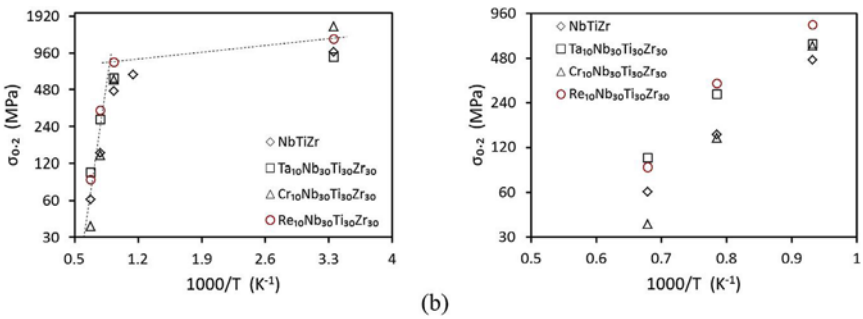

Fig. 13. Arrhenius plots of the yield true stress versus inverse absolute temperature for the studied alloys: (a) the temperature range 250–2000 K, (b) the temperature range 1000–2000 K. Dashed trend lines in figure (a) are for $Re_{10}Nb_{30}Ti_{30}Zr_{30}$.

five elements, i.e. Cr, Fe, Re, Si and W, have limited solubility in NbTiZr, with Si having the smallest and Cr having the largest solubility. At concentrations above the solubility limits of these elements, additional IM phases (Laves or silicide) or a second BCC phase are present, which provides the opportunity for precipitation strengthening at temperatures up to 1400 °C.

2 To verify the results of CALPHAD analysis, three quaternary alloys, $Ta_{10}Nb_{30}Ti_{30}Zr_{30}$, $Cr_{10}Nb_{30}Ti_{30}Zr_{30}$ and $Re_{10}Nb_{30}Ti_{30}Zr_{30}$, were produced and their phase compositions were studied after annealing at 1400 °C and after compression deformation at 800 °C and 1000 °C. Satisfactory agreement between the experimental and calculated results was found.

3 $Ta_{10}Nb_{30}Ti_{30}Zr_{30}$ had essentially single-phase BCC structure and the density of 7.81 g/cm^3. After annealing at 1400 °C the alloy had coarse grains with over 1-mm average diameter. A negligible amount of a Zr-rich second phase was spotted at grain boundaries. At 25 °C the alloy had $\sigma_{0.2} = 882$ MPa and $\varepsilon_f = 64\%$. With an increase in temperature $\sigma_{0.2}$ decreased to 596 MPa at 800 °C, 274 MPa at 1000 °C and 102 MPa at 1200 °C.

4 $Cr_{10}Nb_{30}Ti_{30}Zr_{30}$ had a two-phase, BCC + Laves (C15), structure and the density of 6.56 g/cm^3. The Laves phase was rich in Cr. In the annealed condition the Laves phase was present in the form of needles with a volume fraction of ~5%. High temperature deformation transformed the Laves needles to near-globular particles with a volume fraction of ~7%. At room temperature, the alloy had high yield stress ($\sigma_{0.2} = 1576$ MPa) but low compression ductility ($\varepsilon_f = 5\%$). With an increase in temperature the alloy became ductile and during compression deformation at $T \geq 800$ °C it showed true plastic strain of 70% without any evidence of macroscopic fracture. The yield stress $\sigma_{0.2}$ was 580 MPa at 800 °C, 139 MPa at 1000 °C and 37 MPa at 1200 °C.

5 $Re_{10}Nb_{30}Ti_{30}Zr_{30}$ had a two-phase, BCC + Laves, crystal structure and density of 7.85 g/cm^3. The Laves phase was rich in Re and depleted in Ti and Nb. It was present in the form of cuboidal-shaped precipitates, which volume fraction increased from 5.4% in the annealed condition to ~10% after 1000 °C deformation. The alloy had $\sigma_{0.2} = 1244$ MPa and $\varepsilon_f = 53\%$ at 25 °C. With an increase in temperature $\sigma_{0.2}$ decreased to 805 MPa at 800 °C, 323 MPa at 1000 °C and 89 MPa at 1200 °C.

6 The room temperature strength and hardness of $Cr_{10}Nb_{30}Ti_{30}Zr_{30}$ were higher than those of $Ta_{10}Nb_{30}Ti_{30}Zr_{30}$ and $Re_{10}Nb_{30}Ti_{30}Zr_{30}$. However, with increasing temperature $Cr_{10}Nb_{30}Ti_{30}Zr_{30}$ rapidly lost its strength and at $T \geq 1000$ °C it became softer than the other two quaternary alloys and the ternary NbTiZr alloy. Thus alloying with Cr is not beneficial for high temperature strength.

Acknowledgements

Technical support from S. Boone, W.T. Cissel, L. Griffith, J.M. Scott, P. Fagin and R. Turner is greatly appreciated. Numerous discussions with S.L. Semiatin, D.B. Miracle, K.J. Chaput and T.M. Butler are recognized. Work by O.N. Senkov was supported through the Air Force on-site contract FA8650-15-D-5230 managed by UES, Inc., Dayton, Ohio, United States.

References

[1] D.B. Miracle, O.N. Senkov, A critical review of high entropy alloys and related concepts, Acta Mater. 122 (2017) 448–511.
[2] S. Gorsse, D.B. Miracle, O.N. Senkov, Mapping the world of complex concentrated alloys, Acta Mater. 135 (2017) 177–187.
[3] O.N. Senkov, D.B. Miracle, K.J. Chaput, J.-P. Couzinie, Development and exploration of refractory high entropy alloys: a review, J. Mater. Res. 33 (2018) 3092–3128.
[4] O.N. Senkov, S. Rao, K.J. Chaput, C. Woodward, Compositional effect on microstructure and properties of NbTiZr-based complex concentrated alloys, Acta Mater. 151 (2018) 201–215.
[5] ATI Wah Chang Nb Alloy C-103, in, MatWeb.com, http://www.matweb.com/search/datasheet.aspx?MatGUID=ed50a3a07706450590669cedc7784150.
[6] CompuTherm Software, Databases, in, http://www.computherm.com/index.php?route=product/category&path=59_83.
[7] K.C. Chou, Y.A. Chang, A study of ternary geometrical models, Ber. Bunsenges. Phys. Chem. 93 (1989) 735–741.
[8] K. Wertz, J. Miller, O. Senkov, Toward multi-principal component alloy discovery: assessment of the CALPHAD thermodynamic databases for prediction of novel ternary alloy systems, J. Mater. Res. 33 (2018) 3204–3217.
[9] S. Gorsse, O.N. Senkov, About the reliability of CALPHAD predictions in multicomponent systems, Entropy 20 (2018) 899.
[10] O.N. Senkov, D. Isheim, D.N. Seidman, A.L. Pilchak, Development of a refractory high entropy superalloy, Entropy 18 (2016) 102.
[11] O.N. Senkov, C.F. Woodward, Microstructure and properties of a refractory $NbCrMo_{0.5}Ta_{0.5}TiZr$ alloy, Mater. Sci. Eng. A 529 (2011) 311–320.
[12] K.C.H. Kumar, P. Wollants, L. Delaey, Thermodynamic assessment of the Ti-Zr system and calculation of the Nb-Ti-Zr phase diagram, J. Alloys Compd. 206 (1994) 121–127.
[13] P. Villars, A. Prince, H. Okamoto, Handbook of Ternary Alloy Phase Diagrams, ASM International, Materials Park, OH, USA, 1995.
[14] W. Chen, Q.H. Tang, H. Wang, Y.C. Xie, X.H. Yan, P.Q. Dai, Microstructure and mechanical properties of a novel refractory AlNbTiZr high-entropy alloy, Mater. Sci. Technol. 34 (2018) 1309–1315.
[15] O.N. Senkov, S.V. Senkova, C. Woodward, D.B. Miracle, Low-density, refractory multi-principal element alloys of the Cr–Nb–Ti–V–Zr system: microstructure and phase analysis, Acta Mater. 61 (2013) 1545–1557.
[16] O.N. Senkov, S.V. Senkova, D.B. Miracle, C. Woodward, Mechanical properties of low-density, refractory multi-principal element alloys of the Cr–Nb–Ti–V–Zr system, Mater. Sci. Eng. 565 (2013) 51–62.
[17] T.M. Butler, K.J. Chaput, J.R. Dietrich, O.N. Senkov, High temperature oxidation behaviors of equimolar NbTiZrV and NbTiZrCr refractory complex concentrated alloys (RCCAs), J. Alloys Compd. 729 (2017) 1004–1019.
[18] Y.D. Wu, Y.H. Cai, T. Wang, J.J. Si, J. Zhu, Y.D. Wang, X.D. Hui, A refractory $Hf_{25}Nb_{25}Ti_{25}Zr_{25}$ high-entropy alloy with excellent structural stability and tensile properties, Mater. Lett. 130 (2014) 277–280.
[19] H. Song, F. Tian, D. Wang, Thermodynamic properties of refractory high entropy alloys, J. Alloys Compd. 682 (2016) 773–777.
[20] Y. Zhang, X. Yang, P.K. Liaw, Alloy design and properties optimization of high-entropy alloys, JOM 64 (2012) 830–838.
[21] L.-Y. Tian, G. Wang, J.S. Harris, D.L. Irving, J. Zhao, L. Vitos, Alloying effect on the elastic properties of refractory high-entropy alloys, Mater. Des. 114 (2017) 243–252.
[22] M. Todai, T. Nagase, T. Hori, A. Matsugaki, A. Sekita, T. Nakano, Novel TiNbTaZrMo high-entropy alloys for metallic biomaterials, Scripta Mater. 129 (2017) 65–68.
[23] O.N. Senkov, A.L. Pilchak, S.L. Semiatin, Effect of cold deformation and annealing on the microstructure and tensile properties of a HfNbTaTiZr refractory high entropy alloy, Metall. Mater. Trans. A 49A (2018) 2876–2892.
[24] O.N. Senkov, S.L. Semiatin, Microstructure and properties of a refractory high-entropy alloy after cold working, J. Alloys Compd. 649 (2015) 1110–1123.
[25] B. Schuh, B. Volker, J. Todt, N. Schell, L. Perriere, J. Li, J.P. Couzinie, A. Hohenwarter, Thermodynamic instability of a nanocrystalline, single-phase TiZrNbHfTa alloy and its impact on the mechanical properties, Acta Mater. 142 (2018) 201–212.
[26] N.D. Stepanov, N.Y. Yurchenko, S.V. Zherebtsov, M.A. Tikhonovsky, G.A. Salishchev, Aging behavior of the HfNbTaTiZr high entropy alloy, Mater. Lett. 211 (2018) 87–90.
[27] V. Soni, B. Gwalani, O.N. Senkov, B. Viswanathan, T. Alam, D.B. Miracle, R. Banerjee, Phase stability as a function of temperature in a refractory high-entropy alloy, J. Mater. Res. 33 (2018) 3235–3246.
[28] H.W. Grunling, R. Bauer, The role of silicon in corrosion-resistant high temperature coatings, Thin Solid Films 95 (1982) 3–20.
[29] S.-P. Wang, J. Xu, (TiZrNbTa)-Mo high-entropy alloys: dependence of microstructure and mechanical properties on Mo concentration and modeling of solid solution strengthening, Intermetallics 95 (2018) 59–72.
[30] O.N. Senkov, F. Zhang, J.D. Miller, Phase composition of a $CrMo_{0.5}NbTa_{0.5}TiZr$ high entropy alloy: comparison of experimental and simulated data, Entropy 15 (2013) 3796–3809.
[31] M. Huahai, C. Hai-Lin, C. Qing, TCHEA1: a thermodynamic database not limited for high entropy alloys, J. Phase Equilibria Diffusion 38 (2017) 353–368.
[32] F.G. Coury, T. Butler, K. Chaput, A. Saville, J. Copley, J. Foltz, P. Mason, K. Clarke, M. Kaufman, A. Clarke, Phase equilibria, mechanical properties and design of quaternary refractory high entropy alloys, Mater. Des. 155 (2018) 244–256.
[33] E. Eshed, N. Larianovsky, A. Kovalevsky, V. Popov Jr., I. Gorbachev, V. Popov, A. Katz-Demyanetz, Microstructural evolution and phase formation in 2nd-generation refractory-based high entropy alloys, Materials 11 (2018) 75 (13 pp.).
[34] O.N. Senkov, J.M. Scott, S.V. Senkova, F. Meisenkothen, D.B. Miracle, C.F. Woodward, Microstructure and elevated temperature properties of a refractory TaNbHfZrTi alloy, J. Mater. Sci. 47 (2012) 4062–4074.
[35] G.E. Dieter, H.A. Kuhn, S.L. Semiatin, Handbook of Workability and Process Design, ASM International, Materials Park, OH, USA, 2003.
[36] V. Levitin, High Temperature Strain of Metals and Alloys, Wiley-VCH,

Weinheim, Germany, 2006.
[37] G.E. Dieter, Mechanical Metallurgy, third ed. ed., McGraw-Hill, Inc., NewYork, 1986.
[38] L. Briottet, J.J. Jonas, F. Montheillet, A mechanical interpretation of the activation energy of high temperature deformation in two phase materials, Acta Mater. 44 (1996) 1665–1672.